Geophysical Research Letters

RESEARCH LETTER
10.1029/2025GL117844

Key Points:

- First characterization of year-round nightly-mean Na from 75 to 150 km reveals annual oscillation (AO) and semiannual oscillation (SAO) in Boulder TINa-a summer maximum and spring minimum
- The SAO/AO amplitude ratio profile and maximum thermosphere-ionosphere Na (TINa) contrast to minimum main Na in summer support TINa originated from $TINa^+$ neutralization
- Minimum TINa in spring equinox is linked to minimal wave/eddy transport and meteoric influx hindering $TINa^+$ ion density/upward transport

Supporting Information:

Supporting Information may be found in the online version of this article.

Correspondence to:

X. Chu and Y. Chen,
Xinzhao.Chu@colorado.edu;
Yingfei.Chen@colorado.edu

Citation:

Chu, X., & Chen, Y. (2025). Lidar discovery of annual and semiannual oscillations of thermosphere-ionosphere Na (TINa) layers and the first Na climatology of 75–150 km: Connections to metallic ions, wave and eddy transport, and meteoric influx. *Geophysical Research Letters*, *52*, e2025GL117844. https://doi.org/10.1029/2025GL117844

Received 27 JUN 2025
Accepted 22 AUG 2025

Author Contributions:

Conceptualization: Xinzhao Chu, Yingfei Chen
Data curation: Xinzhao Chu
Formal analysis: Xinzhao Chu, Yingfei Chen
Funding acquisition: Xinzhao Chu
Investigation: Xinzhao Chu, Yingfei Chen
Methodology: Xinzhao Chu, Yingfei Chen

Lidar Discovery of Annual and Semiannual Oscillations of Thermosphere-Ionosphere Na (TINa) Layers and the First Na Climatology of 75–150 km: Connections to Metallic Ions, Wave and Eddy Transport, and Meteoric Influx

Xinzhao Chu[1] and **Yingfei Chen**[1]

[1]Cooperative Institute of Research in Environmental Sciences & Department of Aerospace Engineering Sciences, University of Colorado Boulder, Boulder, CO, USA

Abstract First characterization of year-round Na layers from 75 to 150 km is enabled with 7 years (2011–2017) of high-detection-sensitivity lidar observations over Boulder (40.13°N, 105.24°W). Clear annual and semiannual oscillations (AO and SAO) are revealed in the nightly-mean thermosphere-ionosphere Na (TINa) (~105–150 km) number density and volume mixing ratio with the summer maximum but spring equinox (March/April) minimum. Such stark contrast to the summer minimum in the main Na layers (~75–105 km) supports the theory of TINa formed via $TINa^+$ ion neutralization ($TINa^+ + e^- \rightarrow TINa + h\nu$). The SAO/AO amplitude ratio profiles (75–150 km) exhibit significant changes (~0.06–2), linking TINa SAO to thermospheric density SAO and the minimal wave/eddy transport around midlatitude equinoxes which hinders $TINa^+$ ion production and upward transport via reduced diffusion of the main Na layer. Stronger TINa in autumn than in spring equinox is explained by the maximal (minimal) meteoric influx occurring in September (April).

Plain Language Summary Atmospheric metallic layers in the mesosphere and lower thermosphere (MLT) with altitudes of ~75–105 km have been observed for nearly a century since the 1920s. Studies of their seasonal and diurnal variations as well as vertical and horizontal structures have provided crucial information bearing on the meteoric origin of these metals along with various chemical and dynamical processes in the MLT. However, the existence of neutral metal layers higher up in the thermosphere and ionosphere (E and F regions) was unknown until a lidar discovery of thermosphere-ionosphere metal (TIMt) layers made in Antarctica in 2011 which was followed by numerous observations globally. Sensitive lidar detections of TIMt in Na species (TINa) over Boulder not only led to the discovery of TINa regular occurrence reported earlier but also enable the first-ever study of year-round TINa climatology (~105–150 km) reported here. This study is the first of its kind for characterizing the entire meteoric Na layers from 75 to 150 km. Such studies offer a unique opportunity to explore the fundamental processes and coupling mechanisms in the mesosphere and thermosphere that separate interplanetary space from the lower atmosphere and biosphere, protecting life on Earth.

1. Introduction

The regular occurrence of thermosphere-ionosphere Na (TINa) layers discovered by high-detection-sensitivity Na Doppler lidar observations over Boulder, Colorado (Chen & Chu, 2023; Chu et al., 2021) has significantly augmented the research of thermosphere-ionosphere metal (TIMt) layers, establishing TIMt as excellent tracers for exploring the "thermospheric gap" region around 100–300 km (Oberheide et al., 2011). The initial discovery of TIMt was made in Fe species by Fe Boltzmann lidar observations at McMurdo, Antarctica (Chu et al., 2011), that is, the thermosphere-ionosphere Fe (TIFe) layers named in Chu and Yu (2017). Many following reports of TIMt in K, Na, Fe, and Ca^+ species (termed TIK, TINa, TIFe, and $TICa^+$) and thermosphere-ionosphere sporadic metal (TISMt) layers reveal intriguing features (e.g., Chu et al., 2020; Friedman et al., 2013; Gao et al., 2015; Jiao et al., 2022; Raizada et al., 2015, 2020; Sun et al., 2025; Wu et al., 2022). Most of these events appear to be intermittent except for the reports of TINa from McMurdo and Boulder. While the McMurdo TINa distribute diffusely and persist long beyond TIFe disappearance (Chu et al., 2020), the Boulder TINa layers occur regularly, descending from ~150 km before dawn all year round and from ~125 km after dusk in winter months with semidiurnal tidal phases (Chen & Chu, 2023; Chu et al., 2021). Boulder TINa enables the first investigation of year-round Na layers through the entire altitude range of 75–150 km, which is the subject of this study.

Project administration: Xinzhao Chu
Resources: Xinzhao Chu
Software: Xinzhao Chu, Yingfei Chen
Supervision: Xinzhao Chu
Validation: Xinzhao Chu, Yingfei Chen
Visualization: Xinzhao Chu, Yingfei Chen
Writing – original draft: Xinzhao Chu
Writing – review & editing: Xinzhao Chu, Yingfei Chen

Year-round Na density variations from ~80 to 105 km have been studied extensively at midlatitudes (e.g., Gardner et al., 1986; Gardner & Liu, 2010; Li et al., 2018; She et al., 2000, 2023; States & Gardner, 1999; Yi et al., 2009); however, year-round Na density above 105 km (i.e., TINa layers) had not been reported until this study. The low density of TINa requires very high detection sensitivity (better than 0.1 cm^{-3}) like that of the Na Doppler lidar at Boulder (Chu et al., 2021; Smith & Chu, 2015) but beyond the detection limit (about a few cm^{-3}) of many Na lidars. Regular TINa occurrence and nighttime lidar operation available in every month at Boulder allow reliable measurements of TINa layers all year round. Chen and Chu (2023) reported the annual phase variations of predawn TINa occurring ~2.5 hr earlier in summer than in winter, which closely correlate to annual phase variations of sunrise and semidiurnal tidal winds.

Using the extensive Boulder lidar data set, we characterize variations of Na density and volume mixing ratio (VMR) year-round from 75 to 150 km. An interesting discovery is the semiannual oscillation (SAO) in Na layers and its relative strength to the annual oscillation (AO) varying with altitude from 75 to 150 km, complementing the studies of thermospheric density SAO (e.g., Fuller-Rowell, 1998; Jones et al., 2018; Qian et al., 2009). This investigation provides an opportunity to examine the influences of meteoric influx, chemical processes, wave and eddy transport, and plasma-neutral coupling on atmospheric metals.

2. Year-Round Na Density and Volume Mixing Ratio From 75 to 150 km Over Boulder

Lidar data used in this study were collected from 2011 to 2017 at Table Mountain Observatory (40.13°N, 105.24°W), north of Boulder, with the University of Colorado Boulder Student Training and Atmospheric Research (STAR) Na Doppler lidar (Lu et al., 2015, 2017; Smith & Chu, 2015). While raw photon counts were collected in resolutions of 3 s and 24 m, Na number densities were retrieved with uniform binning of 7.5 min and 960 m to ensure sufficient signal-to-noise ratios (SNRs). Na volume mixing ratios (VMRs) were derived by dividing Na densities with the corresponding atmospheric number densities calculated from the MSISE00 model (Picone et al., 2002). Totally 239 observational nights are used in forming monthly composites after thorough data screening as described in Chen and Chu (2023). All 12 months from January through December have sufficient cases as listed in Table S1 in Supporting Information S1. Each monthly composite of lidar data covering from dusk to dawn is obtained by averaging TINa densities or VMRs of the same local time at the same altitude bin but on different nights within the same month. Monthly composites reduce incoherent features while preserving coherent tidal structures. All monthly composite contours (not shown) exhibit clear signatures of predawn TINa layers, similar as Figure 1 in Chen and Chu (2023).

Monthly profiles of nightly-mean Na densities and VMRs are derived by taking temporal means through the entire nighttime at each altitude of the monthly composites. The raw profiles retrieved to 155 km, are vertically smoothed above ~125 km in a log-10 scale with a 6-km full width (FW) Hamming window first and then smoothed again in the log-10 scale with a 3-km FW Hamming window through the entire altitude range. Such double smooths are to reduce noise at TINa altitudes (~110–150 km) while keeping the main layer's peak, top- and bottom-sides as close to the original profiles as possible. The obtained monthly profiles are shown in Figures 1a and 1b for Na density and VMR, respectively. The raw and smoothed monthly profiles are compared in Figures S1A and S1B in Supporting Information S1 along with the raw standard deviations. Two summer months (June and July) show the maximum TINa densities but the minimum peak Na densities in the main layer. This contrast becomes stronger in VMR (Figure 1b). The April profile exhibits the lowest density/VMR above ~100 km. The raw contours (Figures 1c and 1d) of these monthly composites show the seasonal variations of Na density and VMR through the entire year from 75 to 150 km.

To further quantify such year-round variations, a harmonic fitting consisting of an annual mean (A_0), AO, and SAO, given by Equation 1, is applied to Figures 1c and 1d at each altitude:

$$\text{Na Density or VMR} = A_0 + A_{12}\cos\left[\frac{2\pi}{365}(\text{day} - \text{P}_{12})\right] + A_6\cos\left[\frac{2\pi}{\frac{365}{2}}(\text{day} - P_6)\right]$$

where A_{12} and A_6 are the AO and SAO amplitudes. P_{12} and P_6 are the AO and SAO phases, that is, the day of year corresponding to the maximum Na density or VMR. The fitted values are then subtracted from the original 12

10.1029/2025GL117844

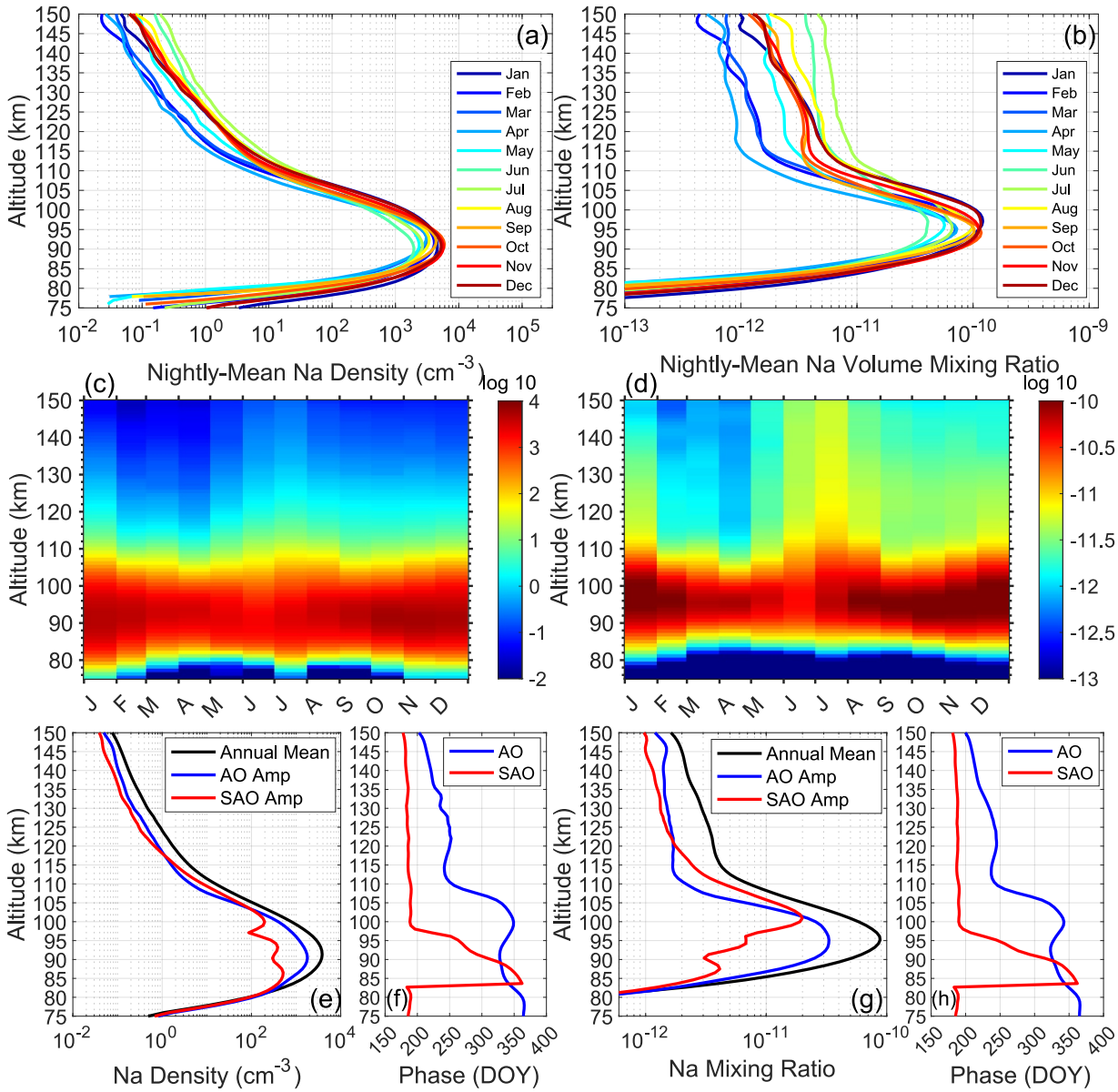

Figure 1. 12 monthly profiles of (a) nightly mean Na density and (b) Na volume mixing ratio (VMR) from January through December. Raw contours of year-round variations of (c) Na density and (d) VMR. Harmonic fitted annual mean, annual oscillation, and semiannual oscillation amplitudes and phases of (e–f) Na density and (g–h) VMR.

monthly profiles, and the resultant residuals are smoothed with a Hamming window of 100-day FW. The smoothed residuals are added back to the fitted values to form the climatology of Na density and VMR from 75 to 150 km. The fitted annual means, AO and SAO amplitudes and phases are plotted for Na density and VMR in Figures 1e–1h. The resultant climatology of Na density and VMR are illustrated in Figures 2a and 2b.

Figure 2 represents the first year-round climatology of Na density and VMR covering the entire altitude range from 75 to 150 km. AO and SAO signatures are clearly shown in TINa density and VMR: Two minima occur around the spring (March-April) and autumn (September-October) equinoxes with spring being the primary minimum, and two maxima occur in summer and winter with summer being the primary maximum. An oval around 115 km spanning from late September to late October in Figure 2b reflects the enhanced Na VMR above the turning point ∼115 km in the monthly profiles of September and October (Figure 1b). The AO phase transitions from November/December in the main layer to late summer (July-August) in TINa (Figures 1f and 1h).

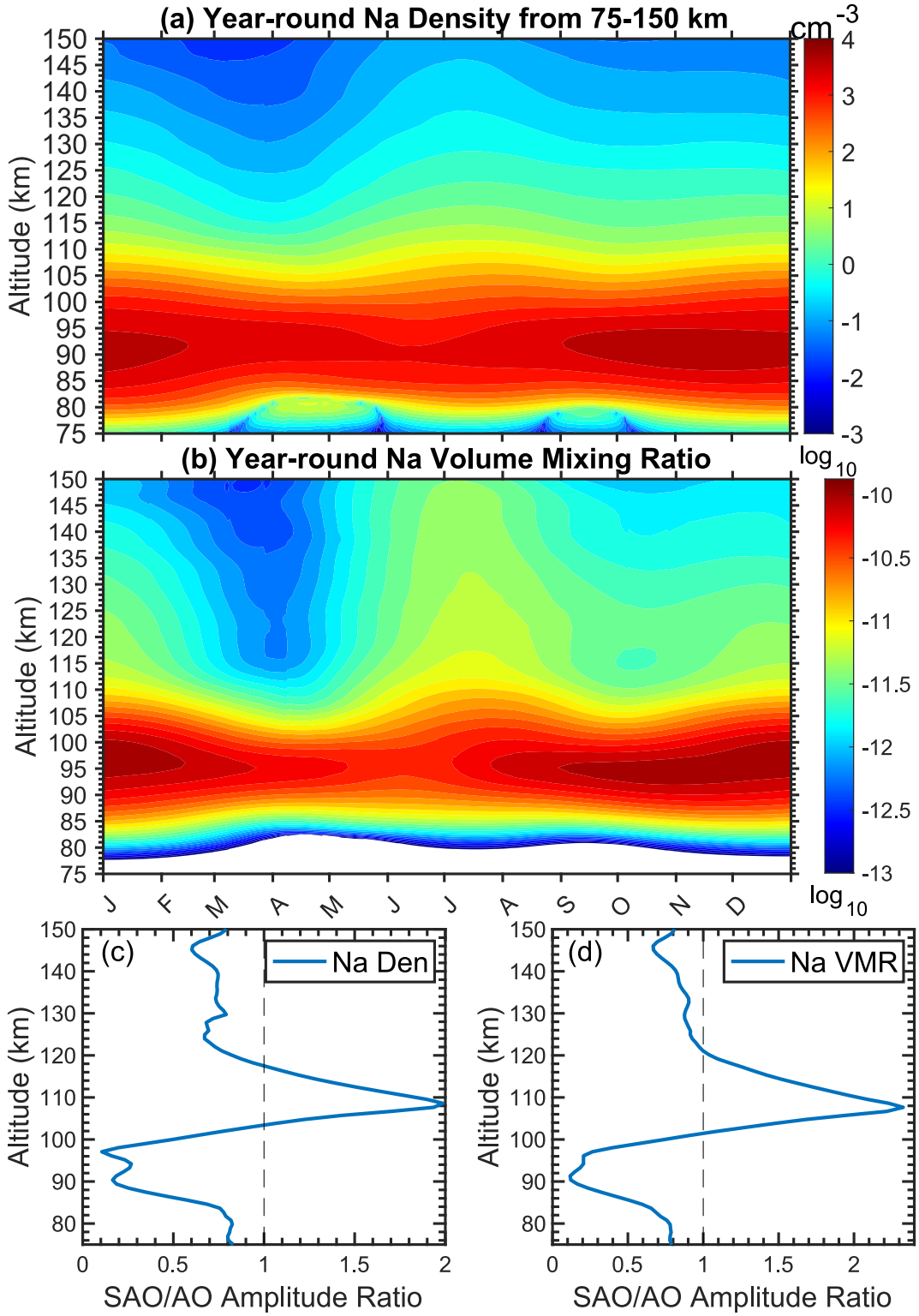

Figure 2. Climatology of year-round nightly-mean (a) Na density and (b) volume mixing ratio (VMR) from 75 to 150 km over Boulder. The semiannual oscillation to annual oscillation amplitude ratio for (c) Na density and (d) VMR from 75 to 150 km.

The SAO phases are in summer (June-July) through most of the altitudes except a gradual phase transition from ~83 to 99 km.

The most salient features in Figure 2 are the SAO of TINa but strong AO of the main Na layer in both density and VMR contours. To quantify the features, the SAO to AO amplitude ratio is computed from the harmonic fitting amplitudes in Figures 1e and 1g for every altitude of Na density and VMR and displayed in Figures 2c and 2d, respectively. The significant changes of the SAO/AO ratio with altitude are stunning, from the minimum ratio of ~0.1 at ~97 km to the maximum of ~1.99 at ~109 km for Na density and ~2.33 at ~108 km for VMR.

1. AO dominates the main Na layer around its density peak (~91.5 km) in ~87–99 km with small SAO/AO ratios (<0.4) where the Na density is mainly controlled by neutral chemical reactions that are highly dependent on the temperature annual variation.
2. The SAO/AO ratio increases rapidly above ~99 km and reaches a peak around 109 km. The ratio exceeds 1 from ~103 to 118 km for Na density and from ~102 to 122 km for VMR, which basically overlaps with the TISMt altitudes (Wu et al., 2022).
3. After decreasing to ~0.7 at 123 km, the SAO/AO ratio profile in Na density turns to be nearly vertical at ~0.7 through the remaining TINa to 150 km while the ratio in VMR is ~0.8 from ~130 to 150 km.
4. Below ~87 km, the SAO/AO ratio increases rapidly and then stabilizes around 0.8 below ~82 km in Na density and VMR.

The annual mean profiles of the nightly-mean Na density and VMR from 75 to 150 km are shown as black curves in Figures 1e and 1g. The Na densities at 105 and 110 km are ~120 and 18 cm^{-3}, comparable to the results of main Na layers reported for nearby locations (She et al., 2023). Above 110 km, the Boulder TINa densities reduce to about 4.0, 1.8, 1.0, 0.5, 0.3, 0.2, and 0.1 cm^{-3} at 115, 120, 125, 130, 135, 140, and 150 km. The annual-mean peak density ~3,840 cm^{-3} of the main Na layer at Boulder is higher than previous reports for midlatitudes but on a par with the trend of Na peak density increase with decade and solar flux reported by She et al. (2023). Note that the annual-mean peak Na density of 3,040 cm^{-3} at Urbana (40°N, 88°W) was obtained during a solar minimum from February 1996 through January 1998 (States & Gardner, 1999), corresponding to the minimal Na abundance in Figure 4b of She et al. (2023) (see Figure S4 in Supporting Information S1). Because Boulder 2011–2017 data is distributed nearly symmetrically around the solar maximum in the 24th solar cycle, the annual mean over these 7 years represents a relatively high level of midlatitude Na, corresponding to the maximal Na abundance in Figure S4b in Supporting Information S1. About 20% increase from the solar minimum (~1996–1997) to the solar maximum (~2012–2015) is consistent with the Na trend inferred from the 28 years of lidar observations (1990–2017) at Fort Collins (41°N, 105°W) and Logan (42°N, 112°W) (She et al., 2023).

3. Characterization of SAO and AO and Connections to Transport, Metallic Ions, and MIF

We compute the column abundance, centroid altitude, and root-mean-square (RMS) width of the main layer (75–105 km) in Figures 3a–3c, along with the TINa column abundance from 150 km downward to 130, 120, 110, and 105 km (Figure 3e). We define the TINa top altitude as the altitude where TINa density drops to 0.20 cm^{-3} or TINa VMR drops to 4.20×10^{-12}, and the Na layer bottom-side altitude at $[Na] = 11\ cm^{-3}$ or VMR $= 1.0 \times 10^{-13}$. The year-round results are plotted in Figures 3f and 3g and overplotted onto the climatology in Figure S2 in Supporting Information S1. The entire Na layer width is calculated as the range from the top to bottom altitudes (Figure 3h). Harmonic fittings are made to Figure 3 parameters using Equation 1 to derive their annual means, AO and SAO amplitudes and phases. The fitted parameters are listed in Table S2 in Supporting Information S1, where the SAO/AO amplitude ratios change from ~0.12 in column abundance to ~2.19 in centroid altitude and to ~3.93 in RMS width of the main Na layer. Besides dominating the RMS width and centroid (Figures 3c–3b), the SAO signatures are obvious in TINa column abundance, Na layer's top and bottom altitudes, and full Na layer range (Figures 3e–3h), and the corresponding SAO/AO amplitude ratios range from ~0.7 to ~1.7 (Table S2 in Supporting Information S1).

Consistent with reports for the main Na layers at Urbana, Fort Collins, and SOR (e.g., Gardner & Liu, 2010; Plane et al., 1999; She et al., 2000; States & Gardner, 1999), AO dominates the main layer's column abundance (Figure 3a) and density variations (Figure 2a) with the minimum in June and maximum in November at Boulder. Such AO was explained by the positive (negative) correlation of Na density with the mesospheric temperature

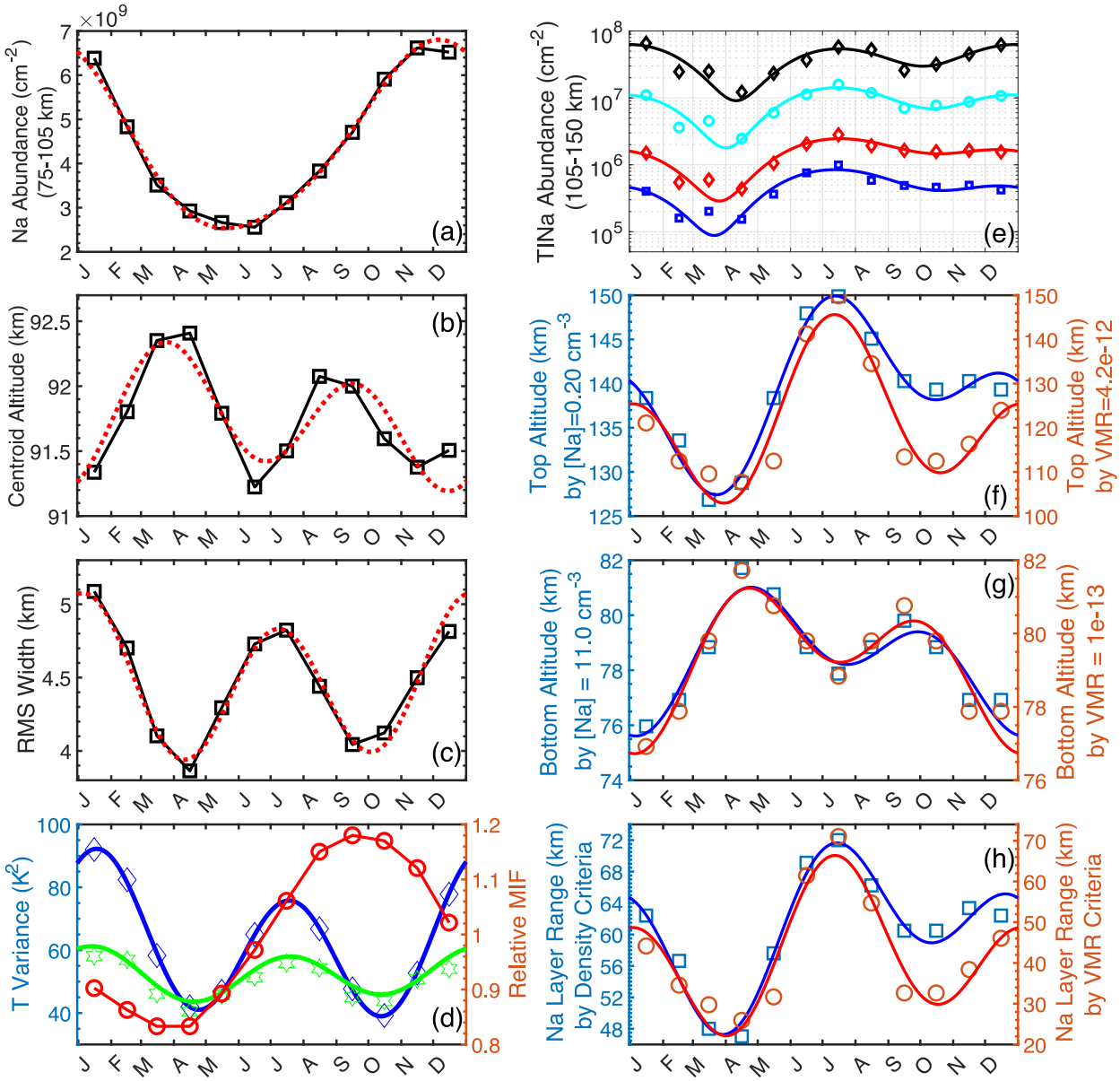

Figure 3. Year-round variations of (a) column abundance, (b) centroid altitude, and (c) RMS width of the main Na layer (75–105 km) at Boulder, (d) wave-induced temperature variance at SOR (blue) and Ft. Collins (green) (Gardner & She, 2022) along with meteoric influx (MIF, red) at 40°N. Year-round variations of (e) thermosphere-ionosphere Na (TINa) column abundance from 150 to 130 (blue), 120 (red), 110 (cyan), and 105 (black) km, (f) TINa top altitude, (g) Na layer bottom altitude, and (h) full Na layer range, determined by density and volume mixing ratio criteria, respectively, over Boulder. Thick, red-dotted curves in (a–c) and thick solid curves in (e–h) are harmonic fittings using Equation 1.

below (above) ~98 km (Plane et al., 1999; States & Gardner, 1999). That is, the cold summer mesopause temperature leads to a large fraction of Na atoms tied up in the $NaHCO_3$ reservoir species below 95 km, while above 98 km the nighttime production of Na via neutralization of Na^+ ions is slowed down by the warm temperature and increased photoionization during summer at the main layer topside. These factors lead to the minimum Na density and column abundance in summer. The opposite occurs in November when the temperature below ~92 km is warmest while the temperature from ~95 to 105 km is colder than other months (Chu et al., 2005), resulting in the maximum Na density and column abundance. Such dominant AO signals help explain the minimal SAO/AO amplitude ratio around the Na layer peak altitude (Figures 2c and 2d).

SAO dominates the main layer's RMS width (Figure 3c) with the narrowest widths at two equinoxes and the variations of centroid altitude (Figure 3b) contain a combination of SAO and AO with the primary and secondary

peaks at the spring and autumn equinoxes, respectively. Plane et al. (1999) state that the SAO signature in the RMS width appears to be consistent with seasonal variations in the vertical eddy diffusivity (Garcia & Solomon, 1985), that is, eddy-induced K_E is large in summer and winter but small at two equinoxes. Gardner and Liu (2007, 2010) point out that gravity-wave-induced dynamical and chemical transport can be much larger than eddy transport by multiple times. The lidar-measured temperature variance Var(T') at SOR and Fort Collins (used to represent wave-induced K_E) is minimum at two equinoxes but at maxima during summer and winter (shown as the blue and green curves in Figure 3d, taken from Gardner and She (2022)). The linear correlation coefficient between the Boulder RMS width and SOR/Fort Collins wave activity Var(T') is 0.90/0.93 at a confidence level of 100%. Basically, weaker wave and eddy transport results in less diffusion and thus less extension of the main Na layer, consequently the narrowest RMS width at two equinoxes as lidar observed at midlatitudes.

The Var(T') averaged from 83 to 103 km at SOR is dominated by SAO with a SAO/AO amplitude ratio of ∼2.63, which is confirmed by lidar data (85–100 km) at Fort Collins from 1996 to 2005, showing a SAO/AO ratio of ∼3.73 (Gardner & She, 2022). The dominant SAO signatures in gravity wave activity are likely responsible for the significant increase of the SAO/AO ratio from ∼100 to 110 km (Figures 2c and 2d). Instead of highly-temperature-dependent chemical reactions controlling the Na density around its layer peak, wave and eddy transport play a key role at the topside of the main Na layer where Na density of 100–110 km mainly comes from the upward diffusion of main Na layer, although ion-molecular chemistry starts to become effective (Plane et al., 2015). Therefore, the minimal wave transport at equinoxes leads to minimal Na density in 100–110 km twice a year, resulting in the strongest SAO signature. Although the SAO/AO ratio still exceeds 1, the quick decrease of SAO/AO ratio from ∼109 to ∼120 km suggests that the production of TINa from neutralization of $TINa^+$ ions starts to compete well with the wave and eddy transport effect above 110 km. Once above ∼120 km, direct neutral transport of Na atoms by wave and eddy and dissociative recombination of $TINa^+$ ions cease functioning but the production of TINa via $TINa^+ + e^- \rightarrow TINa + h\nu$ dominates the TINa density. The TINa SAO above 120 km most likely results from $TINa^+$ ion density and transport affected by the wave activity SAO (see Section 4), leading to a SAO/AO ratio balanced at ∼0.7. Approaching the Na layer bottom-side (below the peak), wave transport SAO affects both the layer bottom altitude (thus the RMS width) via diffusion and many neutral species including atomic O and Na species. A balance between the dynamical transport (wave and eddy) and chemical transport (chemical production and loss of Na that is affected by the atomic oxygen shelf) likely leads to a SAO/AO ratio of ∼0.8. These qualitative explanations of the observed SAO/AO amplitude ratios should be verified by future numerical simulations.

The TINa top altitude (Figure 3g) determined from Na density shows both AO and SAO signatures with the lowest value (∼127 km) in March/April but the highest in July (∼150 km). The top altitude determined from VMR reveals even stronger SAO—the lowest heights ∼108–112 km at two equinoxes and ∼150 km highest in July. Since the wave-induced transport is proportional to $-K_{\mathrm{Wave}} \cdot \partial \overline{\rho}_C / \partial z$, where K_{Wave} is the effective wave-induced diffusivity and $\partial \overline{\rho}_C / \partial z$ is the vertical gradient of mean density of constituent (Gardner, 2024), while inducing upward transport of Na on the topside of the main Na layer (above ∼100 km), the strong wave activity in summer induces downward transport of O from the middle-upper thermosphere to the lower thermosphere, which decreases the thermospheric mass and number densities at TINa altitudes (below 200 km) in summer. Figure S3b in Supporting Information S1 illustrates the year-round total number density, molecular nitrogen (N_2), and atomic oxygen (O) at 130 km provided by MSISE00. The total number density reaches two minima in summer and winter while two maxima in April and October. Such thermospheric density SAO signals help enhance two summer and winter maxima and two equinox minima of TINa VMR when it is derived from dividing TINa density with total thermospheric density. The lidar-measured wave transport lends support to modeling studies suggesting that thermospheric density SAO is mainly induced by the lower atmosphere SAO (e.g., Jones et al., 2017, 2018; Pilinski & Crowley, 2015; Qian et al., 2009; Qian & Yue, 2017).

TINa are unlikely to be formed by direct transport of neutral Na atoms as concluded in earlier studies (Chen & Chu, 2023; Chu et al., 2020, 2021). This is because Na VMR profiles of individual nights show enhanced mixing ratios at TINa altitudes above a turning point, invoking in situ generation of TINa via neutralization of converged $TINa^+$ ($TINa^+ + e^- \rightarrow TINa + h\nu$) (Chen & Chu, 2023; Chu et al., 2021). This conclusion is supported by the reduced summer wave activity in recent decades due to the megadrought in Southwestern North America (Gardner & She, 2022). The winter wave activity is higher than the summer wave activity at both SOR and Ft.

Collins: SOR winter is somewhat higher in 1998–2000 while Ft. Collins is much higher after 2000 (see Figure S3a in Supporting Information S1). This wave situation is opposite to the observed summer TINa being stronger and extends to higher altitude than those for winter TINa. Thus, eddy and wave-induced transport of neutrals (metals and atomic O) alone cannot explain the observed TINa AO and SAO. The opposite density extremes of TINa (maximum) and main Na (minimum) in summer further support the hypothesis of TINa production via $TINa^+$ neutralization. Moreover, electron density in the night maximizes in summer but minimizes in winter over Boulder by a factor of ∼2 (Figure S3b in Supporting Information S1), which helps expedite TINa production via recombination of $TINa^+$ with electrons in summer, resulting in stronger TINa in summer than in winter as observed.

4. Discussion and Conclusions

Synthesizing all factors above, we propose a hypothesis to explain the observed TINa AO and SAO over Boulder. This hypothesis is based on the basic understanding that $TINa^+$ ions dominate the Na chemistry and transport process in the E-F regions and neutral TINa atoms are produced from neutralization of $TINa^+$, serving as a tracer in the thermospheric gap region.

1. Strong wave-induced transport and eddy diffusion in summer and winter helps extend the main layer's topside, not only leading to the wider width of main layer (Figure 3c) but also enabling production of more Na^+ via charge transfer with main ions NO^+ and $O_2{}^+$ around 100–110 km during daytime (Plane et al., 2015). More photoionization due to longer sunlit time in summer also helps keep higher concentrations of ions and electrons than other seasons, including winter which experiences minimal electron density after midnight.
2. The minimal wave-induced and eddy transport around two equinoxes causes the main Na layer to have narrower width and lower upward extension, thus substantial reduction of Na^+ density in 100–110 km as daytime photoionization rate decreases with decreasing altitude.
3. Because the ion drift velocity in the E–D region decreases with decreasing altitude due to increased ion-neutral collision frequency (see Equation 2–4 in Chen and Chu (2023) and Figure 3a in Chu et al. (2021)), the higher altitude and density of Na^+ ions in summer and winter enhance upward transport of Na^+ by electric fields and neutral winds (Chu & Yu, 2017), leading to higher $TINa^+$ density and altitude in the E–F regions. Combined with the enhanced electron density, recombination of converged $TINa^+$ with electrons during nighttime is more efficient in summer than in winter, leading to TINa density and altitude peaking in summer.
4. The reduced density and lower altitude of Na^+ at the main-layer topside around equinoxes result in significantly weaker upward transport of Na^+ due to the increased ion-neutral collisions at lower altitudes. Consequently, much less $TINa^+$ ion density presents in the *E* region, leading to lower TINa density and altitude around equinoxes.
5. The meteoric influx is minimized around the spring equinox while maximized around the autumn equinox (Carrillo-Sánchez et al., 2016), leading to the overall column abundance of Na and Na^+ being minimal around the spring equinox. This MIF factor contributes to the observed TINa being weakest in spring but much stronger in autumn.

In conclusion, the first characterization of year-round Na layers through the entire altitude range of 75–150 km is enabled with 7 years (2011–2017) of high-detection-sensitivity Na Doppler lidar observations over Boulder (40.13°N, 105.24°W). Clear AO and SAO are revealed in the nightly-mean TINa (∼105–150 km) number density and VMR with the maximum in summer but minimum around spring equinox (March/April). The results are in stark contrast to the summer minimum and winter maximum in the main Na layers (∼75–105 km), supporting the $TINa^+$ ion-neutralization origin of TINa ($TINa^+ + e^- \rightarrow TINa + h\nu$). The SAO/AO amplitude ratio profiles (75–150 km) exhibit large changes from a minimum of ∼0.1 at ∼97 km to a maximum of ∼2.0/2.3 at ∼109 km for Na density/VMR. The significant increase of SAO/AO ratio from ∼100 to 110 km is most likely linked to the minimal wave/eddy transport around midlatitude equinoxes. The minimal wave/eddy transport leads to the minimal upward diffusion of main Na layers, which results in the minimal Na density in 100–110 km twice a year and hinders $TINa^+$ ion production and upward transport around equinoxes. Above ∼110 km, the SAO/AO ratio decreases from its peak value to ∼0.7/0.8 for TINa density/VMR in 130–150 km, also suggesting the TINa origin of in situ production from $TINa^+$ neutralization, not the direct transport of neutral Na. The SAO in TINa VMR is linked to the thermospheric density SAO that is also likely caused by the minimal wave/eddy transport around midlatitude equinoxes. TINa being stronger around autumn than spring equinox is likely explained by the maximal and minimal meteoric input fluxes (MIF) occurring in September and April, respectively. Despite the

maximum wave transport of main Na layer occurring in winter, the minimum electron density in winter nighttime hinders the production of TINa via electron recombination with $TINa^+$ ions, causing winter TINa peak being secondary when compared to the primary maximum in summer.

The hypothesis above should be tested with model simulations integrating all factors (including tidal winds and electric fields) together. The obvious change of Na density scale height around 115 km (Figure 1) indicates different formation mechanisms dominating the regions above and below ∼115 km, supporting the hypothesis above and deserving future studies. The Na VMR annual contour/mean are the first of its kind published from observations, serving as references for model validations. Although the annual-mean TINa density is ∼0.1 cm^{-3} near 150 km, modern Na Doppler lidars can still detect them well. If equipped with larger telescopes and more powerful lasers, it is possible to measure temperatures, winds, and waves in the thermospheric gap region from 100 to 200 km with high-sensitivity Na Doppler lidars.

Data Availability Statement

The data shown in this work can be downloaded in MatLab data format from Mendeley Data repository https://data.mendeley.com/datasets/95jh5rt246/2 (Chu & Chen, 2025).

Acknowledgments
We are grateful to Dr. John Plane, Dr. Wuhu Feng, Dr. Chester S. Gardner, and Dr. Liying Qian for providing the MIF data and for invaluable discussions on metal layers, wave-induced transport, and thermospheric density variations. We thank Wentao Huang, Weichun Fong, John Smith, Zhibin Yu, Cao Chen, Zhangjun Wang, Xianxin Li, Chao Chen, Yuli Han, Jian Zhao, and Zhengyu Hua for their contributions to the STAR lidar development, receiver improvement, and/or data collection at Boulder. This work was supported by NSF Grants AGS-2330168 and OPP-2110428. Yingfei Chen is grateful to generous support of Cooperative Institute for Research in Environmental Sciences (CIRES) Graduate Student Research Award and Reid Memorial Scholarship.

References

Carrillo-Sánchez, J. D., Nesvorný, D., Pokorný, P., Janches, D., & Plane, J. M. C. (2016). Sources of cosmic dust in the Earth's atmosphere. *Geophysical Research Letters*, *43*, 11979–11986. https://doi.org/10.1002/2016GL071697

Chen, Y., & Chu, X. (2023). Lidar observations of predawn thermosphere-ionosphere Na (TINa) layers over boulder (40.13°N, 105.24°W): Annual phase variations and correlation with sunrise and tidal winds. *Geophysical Research Letters*, *50*(18), e2023GL105626. https://doi.org/10.1029/2023GL105626

Chu, X., & Chen, Y. (2025). Lidar discovery of annual and semiannual oscillations of thermosphere-ionosphere Na (TINa) layers and the first Na climatology of 75–150 km: Connections to metallic ions, wave and eddy transport, and meteoric influx (version 2) [Dataset]. *Mendeley Data*. https://data.mendeley.com/datasets/95jh5rt246/2

Chu, X., Chen, Y., Cullens, C. Y., Yu, Z., Xu, Z., Zhang, S., et al. (2021). Mid-Latitude thermosphere-ionosphere Na (TINa) layers observed with high-sensitivity Na Doppler Lidar over boulder (40.13°N, 105.24°W). *Geophysical Research Letters*, *48*(11), 1–10. https://doi.org/10.1029/2021GL093729

Chu, X., Gardner, C. S., & Franke, S. J. (2005). Nocturnal thermal structure of the mesosphere and lower thermosphere region at Maui, Hawaii (20.7°N), and Starfire Optical Range, New Mexico (35°N). *Journal of Geophysical Research*, *110*(D9), D09S03. https://doi.org/10.1029/2004JD004891

Chu, X., Nishimura, Y., Xu, Z., Yu, Z., Plane, J. M. C., Gardner, C. S., & Ogawa, Y. (2020). First simultaneous lidar observations of thermosphere-ionosphere Fe and Na (TIFe and TINa) layers at McMurdo (77.84°S, 166.67°E), Antarctica with Concurrent measurements of Aurora activity, enhanced Ionization layers, and converging electric field. *Geophysical Research Letters*, *47*(20), e2020GL090181. https://doi.org/10.1029/2020GL090181

Chu, X., & Yu, Z. (2017). Formation mechanisms of neutral Fe layers in the thermosphere at Antarctica studied with a thermosphere-ionosphere Fe/Fe+ (TIFe) model. *Journal of Geophysical Research: Space Physics*, *122*(6), 6812–6848. https://doi.org/10.1002/2016JA023773

Chu, X., Yu, Z., Gardner, C. S., Chen, C., & Fong, W. (2011). Lidar observations of neutral Fe layers and fast gravity waves in the thermosphere (110-155 km) at McMurdo (77.8°S, 166.7°E), Antarctica. *Geophysical Research Letters*, *38*(23), 1–6. https://doi.org/10.1029/2011GL050016

Friedman, J. S., Chu, X., Brum, C., & Lu, X. (2013). Observation of a thermospheric descending layer of neutral K over Arecibo. *Journal of Atmospheric and Solar-Terrestrial Physics*, *104*, 253–259. https://doi.org/10.1016/j.jastp.2013.03.002

Fuller-Rowell, T. J. (1998). The "thermospheric spoon": A mechanism for the semiannual density variation. *Journal of Geophysical Research*, *103*(A3), 3951–3956. https://doi.org/10.1029/97JA03335

Gao, Q., Chu, X., Xue, X., Dou, X., Chen, T., & Chen, J. (2015). Lidar observations of thermospheric Na layers up to 170 km with a descending tidal phase at Lijiang (26.7°N, 100.0°E), China. *Journal of Geophysical Research: Space Physics*, *120*(10), 9213–9220. https://doi.org/10.1002/2015JA021808

Garcia, R. R., & Solomon, S. (1985). The effect of breaking gravity waves on the dynamics and chemical composition of the mesosphere and lower thermosphere. *Journal of Geophysical Research*, *90*(D2), 3850–3868. https://doi.org/10.1029/JD090iD02p03850

Gardner, C. S. (2024). Impact of atmospheric Compressibility and Stokes drift on the vertical transport of heat and constituents by gravity waves. *Journal of Geophysical Research: Atmospheres*, *129*(8), e2023JD040436. https://doi.org/10.1029/2023JD040436

Gardner, C. S., & Liu, A. Z. (2007). Seasonal variations of the vertical fluxes of heat and horizontal momentum in the mesopause region at Starfire Optical Range, New Mexico. *Journal of Geophysical Research*, *112*(D9), D09113. https://doi.org/10.1029/2005JD006179

Gardner, C. S., & Liu, A. Z. (2010). Wave-induced transport of atmospheric constituents and its effect on the mesospheric Na layer. *Journal of Geophysical Research*, *115*(D20), D20302. https://doi.org/10.1029/2010JD014140

Gardner, C. S., & She, C. Y. (2022). Signature of the Contemporary Southwestern North American megadrought in mesopause region wave activity. *Geophysical Research Letters*, *49*(19), 1–8. https://doi.org/10.1029/2022GL100569

Gardner, C. S., Voelz, D. G., Sechrist, C. F., Jr., & Segal, A. C. (1986). Lidar studies of the nighttime sodium layer over Urbana, Illinois: 1. Seasonal and nocturnal variations. *Journal of Geophysical Research*, *91*(A12), 13659–13673. https://doi.org/10.1029/JA091iA12p13659

Jiao, J., Chu, X., Jin, H., Wang, Z., Xun, Y., Du, L., et al. (2022). First lidar profiling of meteoric Ca + ion transport from ∼80 to 300 km in the midlatitude nighttime ionosphere. *Geophysical Research Letters*, *49*(18), e2022GL100537. https://doi.org/10.1029/2022gl100537

Jones, M., Emmert, J. T., Drob, D. P., & Siskind, D. E. (2017). Middle atmosphere dynamical sources of the semiannual oscillation in the thermosphere and ionosphere. *Geophysical Research Letters*, *44*(1), 12–21. https://doi.org/10.1002/2016GL071741

Jones, M., Jr., Emmert, J. T., Drob, D. P., Picone, J. M., & Meier, R. R. (2018). Origins of the thermosphere-ionosphere semiannual oscillation: Reformulating the "thermospheric spoon" mechanism. *Journal of Geophysical Research: Space Physics*, *123*(1), 931–954. https://doi.org/10.1002/2017JA024861

Li, T., Ban, C., Fang, X., Li, J., Wu, Z., Feng, W., et al. (2018). Climatology of mesopause region nocturnal temperature, zonal wind and sodium density observed by sodium lidar over Hefei, China (32° N, 117° E). *Atmospheric Chemistry and Physics*, *18*(16), 11683–11695. https://doi.org/10.5194/acp-18-11683-2018

Lu, X., Chen, C., Huang, W., Smith, J. A., Chu, X., Yuan, T., et al. (2015). A coordinated study of 1 h mesoscale gravity waves propagating from Logan to Boulder with CRRL Na Doppler lidars and temperature mapper. *Journal of Geophysical Research: Atmosphere*, *120*(19), 10006–10021. https://doi.org/10.1002/2015JD023604

Lu, X., Chu, X., Li, H., Chen, C., Smith, J. A., & Vadas, S. L. (2017). Statistical characterization of high-to-medium frequency mesoscale gravity waves by Lidar-measured vertical winds and temperatures in the MLT. *Journal of Atmospheric and Solar-Terrestrial Physics*, *162*, 3–15. https://doi.org/10.1016/j.jastp.2016.10.009

Oberheide, J., Forbes, J. M., Zhang, X., & Bruinsma, S. L. (2011). Climatology of upward propagating diurnal and semidiurnal tides in the thermosphere. *Journal of Geophysical Research*, *116*(A11), A11306. https://doi.org/10.1029/2011JA016784

Picone, J. M., Hedin, A. E., Drob, D. P., & Aikin, A. C. (2002). NRLMSISE-00 empirical model of the atmosphere: Statistical comparisons and scientific issues. *Journal of Geophysical Research*, *107*(A12), 1–16. https://doi.org/10.1029/2002JA009430

Pilinski, M. D., & Crowley, G. (2015). Seasonal variability in global eddy diffusion and the effect on neutral density. *Journal of Geophysical Research: Space Physics*, *120*(4), 3097–3117. https://doi.org/10.1002/2015JA021084

Plane, J. M. C., Feng, W., & Dawkins, E. C. M. (2015). The mesosphere and metals: Chemistry and changes. *Chemical Reviews*, *115*(10), 4497–4541. https://doi.org/10.1021/cr500501m

Plane, J. M. C., Gardner, C. S., Yu, J., She, C. Y., Garcia, R. R., & Pumphrey, H. C. (1999). Mesospheric Na layer at 40°N: Modeling and observations. *Journal of Geophysical Research*, *104*(D3), 3773–3788. https://doi.org/10.1029/1998JD100015

Qian, L., Solomon, S. C., & Kane, T. J. (2009). Seasonal variation of thermospheric density and composition. *Journal of Geophysical Research*, *114*(A1), A01312. https://doi.org/10.1029/2008JA013643

Qian, L., & Yue, J. (2017). Impact of the lower thermospheric winter-to-summer residual circulation on thermospheric composition. *Geophysical Research Letters*, *44*(9), 3971–3979. https://doi.org/10.1002/2017GL073361

Raizada, S., Brum, C. M., Tepley, C. A., Lautenbach, J., Friedman, J. S., Mathews, J. D., et al. (2015). First simultaneous measurements of Na and K thermospheric layers along with TILs from Arecibo. *Geophysical Research Letters*, *42*(23), 10106–10112. https://doi.org/10.1002/2015GL066714

Raizada, S., Smith, J. A., Lautenbach, J., Aponte, N., Perillat, P., Sulzer, M., & Mathews, J. D. (2020). New lidar observations of Ca+ in the mesosphere and lower thermosphere over Arecibo. *Geophysical Research Letters*, *47*(5), 1–9. https://doi.org/10.1029/2020GL087113

She, C. Y., Chen, S., Hu, Z., Sherman, J., Vance, J. D., Vasoli, V., et al. (2000). Eight-year climatology of nocturnal temperature and sodium density in the mesopause region (80 to 105 km) over Fort Collins, CO (41°N, 105°W). *Geophysical Research Letters*, *27*(20), 3289–3292. https://doi.org/10.1029/2000GL003825

She, C. Y., Krueger, D. A., Yan, Z. A., Yuan, T., & Smith, A. K. (2023). Climatology, long-term trend and solar response of Na density based on 28 Years (1990–2017) of midlatitude mesopause Na lidar observation. *Journal of Geophysical Research: Space Physics*, *128*(11), 1–13. https://doi.org/10.1029/2023JA031652

Smith, J. A., & Chu, X. (2015). High-efficiency receiver architecture for resonance-fluorescence and Doppler Lidars. *Applied Optics*, *54*(11), 3173–3184. https://doi.org/10.1364/AO.54.003173

States, R. J., & Gardner, C. S. (1999). Structure of the mesospheric Na layer at 40°N latitude: Seasonal and diurnal variations. *Journal of Geophysical Research*, *104*(D9), 11783–11798. https://doi.org/10.1029/1999JD900002

Sun, W., Jiao, J., Yang, G., Li, G., Xie, H., Zhao, B., et al. (2025). First observation of ionospheric plasma Bubble signatures by Ca+ Lidar at low latitude. *Geophysical Research Letters*, *52*(6), e2025GL114696. https://doi.org/10.1029/2025GL114696

Wu, F., Chu, X., Du, L., Jiao, J., Zheng, H., Xun, Y., et al. (2022). First simultaneous lidar observations of thermosphere-ionosphere sporadic Ni and Na (TISNi and TISNa) layers (∼105–120 km) over Beijing (40.42°N, 116.02°E). *Geophysical Research Letters*, *49*(16), e2022GL100397. https://doi.org/10.1029/2022gl100397

Yi, F., Yu, C., Zhang, S., Yue, X., He, Y., Huang, C., et al. (2009). Seasonal variations of the nocturnal mesospheric Na and Fe layers at 30°N. *Journal of Geophysical Research*, *114*(D1), D01301. https://doi.org/10.1029/2008JD010344